Springer

Available online at https://link.springer.com/journal/42241
http://www.jhydrodynamics.com
Journal of Hydrodynamics, 2022, 34(3): 499-509
https://doi.org/10.1007/s42241-022-0038-z

Effects of cavitation on vortex-induced vibration of a flexible circular cylinder simulated by fluid-structure interaction method

Zhi-jian Xiao[1], Shi-hao Yang[2], Cao Yu[3], Zhen Zhang[4], Lei Sun[2], Jiang Lai[2*], Yan-ping Huang[2]
1. *Key Laboratory for Mechanics in Fluid Solid Coupling Systems, Institute of Mechanics, Chinese Academy of Sciences, Beijing 100190, China*
2. *Nuclear Power Institute of China, Chengdu 610041, China*
3. *Beijing Electro-mechanical Engineering Institute, Beijing 100074, China*
4. *State Key Laboratory of Mechanical Behavior and System Safety of Traffic Engineering Structures, Shijiazhuang Tiedao University, Shijiazhuang 050043, China*

(Received January 13, 2022, Revised March 7, 2022, Accepted March 30, 2022, Published online June 23, 2022)
©China Ship Scientific Research Center 2022

Abstract: To investigate the effects of the cavitation on the vortex-induced vibration (VIV), the flow and the vibration characteristics of a flexible circular cylinder in the non-cavitating and cavitating flows at $Re = 200$ are simulated using a fluid-structure interaction (FSI) solver, developed in the OpenFOAM framework. The accuracy of the FSI solver is verified using the benchmark cases. For a freely vibrating circular cylinder, the characteristics of the VIV are determined at different frequency ratios. The frequency lock-in is observed in both the cavitating flow and the non-cavitating flow, and the lock-in frequency range is larger in the cavitating flow with a smaller vibration amplitude. In the lock-in frequency range, due to the reduction of the fluid forces and the resonance effects at the dominant frequency, the vibration amplitude is decreased in the cavitating flow, as compared to the non-cavitating flow. Moreover, the low-density vapor and the cavitation collapse weaken the constraints of the flow and the stability of the shedding vortices, respectively, making the flow around the circular cylinder more sensitive to the structural vibration. Consequently, the lock-in frequency range is larger in the cavitating flow.

Key words: Fluid-structure interaction (FSI), cavitation, lock-in frequency, vortex-induced vibrations, OpenFOAM

Introduction

With the development of the marine equipment and the hydraulic machinery, such as the high-speed underwater axi-symmetrical vehicles[1], the marine risers[2] and the flow pumps[3], the structural dynamic response in the cavitating flow becomes an issue of extensive attention. The characteristics of the fluid-structure interaction (FSI) systems are a key factor affecting the safety and the operability of these devices. Meanwhile, the various simulation technologies[4-5] are playing an important role in the design and the evaluation of the FSI systems.

In recent years, two typical geometric configurations, the circular cylinder and the hydrofoil, are often used to study the vortex induced vibration (VIV) under different conditions[6-8]. The VIV of a circular cylinder was widely studied under different conditions in the fully wetted flows[9-10], but not so much in the cavitating flows. Shi et al.[11] used the arbitrary Lagrangian-Eulerian methods to investigate the effects of the head shape and the material elasticity of a circular cylinder on its structural deformation. It is shown that the structure deformation near the cavitating area increases when the cone angle of the head shape increases. Sun et al.[12] investigated the vibration and the deformation of a circular cylinder entering the water at a high speed and it was shown that the hydrodynamic load is the largest at the time of the impact on the free surface. Gao et al.[13] analyzed the entry of a flexible circular cylinder into the water using numerical simulations and it was shown that the water-entry speed is closely related to the cavity closure and the hydrodynamic load. The peak hydrodynamic load on the flexible circular cylinder was found to be smaller than that on a rigid one. These studies mentioned above were mainly focused on the structural hydroelasticity response in the cavitating flow, without adequately considering the

Project supported by the National Natural Science Foundation of China (Grant Nos. 12072336, 12122214).
Biography: Zhi-jian Xiao (1992-), Male, Master,
E-mail: xiaozhijian@imech.ac.cn
Corresponding author: Jiang Lai
E-mail: laijiang1983@163.com

interaction between the cavitation and the VIV.

As the cavitation and the FSI often occur in the hydraulic machinery at the same time, meanwhile, the hydrofoil is a simplified model of the rotating blades, the VIV in the cavitating flow was widely studied by taking the hydrofoils as the object. Kaolan et al.[14] observed experimentally that the hydrofoil shows a flutter-like behavior when the cavity length almost reaches the chord length in the super-cavitating flow. Akcabay et al.[15] showed that the vibrating fluctuation of the structures in a super-cavitating flow is similar to that in a fully wetted flow. Resonances occur when the pitching frequency of a hydrofoil is close to the cavity breakdown frequency[16]. Sareen et al.[17] showed that the vibration amplitudes significantly increase when the cavity shedding frequencies are close to the natural vibrating frequencies of the structures. Torre et al.[18] found that the natural vibrating frequencies of the hydrofoil decrease when the fluid is changed from a still water to a cavitating flow. Ducoin et al.[19] studied experimentally the stationary and pitching flexible hydrofoils in the cavitating flow. Their observations showed that the collapse of the cloud cavity would excite the wetted natural vibrating frequencies of the hydrofoil.

These studies help the understanding of the interaction between the cavitation and the structural vibration, but not so much quantitatively. This paper focuses on the effect of the cavitation on the VIV for different frequency ratios F^* (i.e., the ratio of the dry natural vibrating frequency F_s to the vortex shedding frequency F_L).

The numerical simulations are conducted using an in-house FSI solver in the OpenFOAM framework. The FSI solver consists of a multiphase-flow solver based on the incompressible Navier-Stokes equations and a structural solver based on the rigid-body motion equations. The accuracy of the solver is verified using the benchmark cases. We investigate the VIV of a freely vibrating circular cylinder in the non-cavitating and cavitating flows in the range $(F^* = 0.5\text{-}3.5)$. The vibrating frequency and amplitude of the structure in the lock-in frequency range are analyzed to see the effects of the cavitation on the VIV.

1. Numerical method

1.1 *FSI technique*

The numerical approach adopted in this paper couples an in-house FSI solver, developed by the authors in the framework OpenFOAM, with a multi-phase flow solver for the incompressible Navier-Stokes equations and a structural solver for the rigid-body motion equations. A dynamic mesh is adopted, using the class dynamicMotionSolverFvMesh in the OpenFOAM. The characteristics of the flow past a circular cylinder are predicted by the fluid solver using a large eddy simulation (LES), a volume of fluid (VOF) model and a Kunz cavitation model based on the mass transfer. The transient vibration of the circular cylinder is obtained by solving the governing equations for the rigid-body motion using the structural solver with a fourth-order Runge Kutta method (RK4) and a Newmark method.

A loose coupling method is applied as the FSI model in this paper, which involves a partitioned FSI algorithm and decouples the relatively independent structural and multiphase flow solvers. In view of the lags between the outputs from the structural and fluid solvers in the high frequency pulsation induced by the cavitation, the time step is set as 0.0001 s, which ensures that the courant number remains less than 0.5 on all grids and enables high-accuracy solutions to be obtained within a reasonable time. Information is exchanged between the fluid flow and the structural motion at each time step, in which the explicit time advance is adopted. A spring mesh reconstruction method is used to model the dynamic boundary of the flow field. The whole numerical procedure is illustrated in Fig. 1.

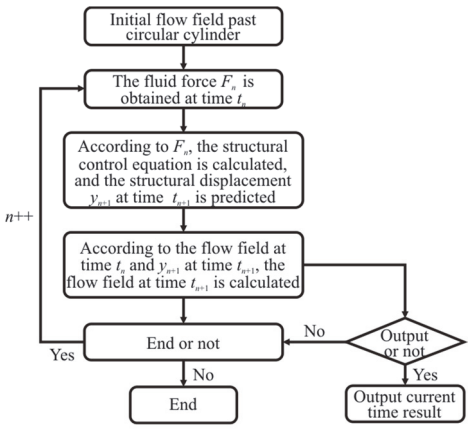

Fig. 1 The procedures of numerical solutions

1.2 *Fluid model*

The unsteady Navier-Stokes equations are solved by using the LES method and a mass transfer cavitation model. In the unsteady cavitating flow, the transition between the liquid and the vapor is complex. The mass transfer rate is obtained using the Kunz cavitation model[20]:

$$\dot{m}^+ = \frac{C_v \rho_v \alpha \min[0, \overline{p} - p_v]}{(1/2\rho_l U_\infty^2) t_\infty}, \quad \dot{m}^- = \frac{C_c \rho_v \alpha^2 (1-\alpha)}{t_\infty} \tag{1}$$

where p_v is the saturated vapor pressure of the water, with a value of 2 438 Pa in this paper. m^+ is the

evaporation rate, m^- is the condensation rate, U_∞ is the velocity of the free stream and t_∞ is the characteristic time. The empirical constants for different phase transfer rates are set as $C_v = 200$, $C_c = 200$, based on the similar previous computational research[21].

The viscous flow field is simulated using an LES turbulence model, where the large-scale eddies are simulated by solving the instantaneous Navier-Stokes equations directly, while the small-scale eddies are simulated by a sub-grid scale (SGS) model. The SGS model and the filter function used to distinguish the large-scale eddies from the small-scale eddies are the two key components in the LES method. A physical parameter $u_i(r)$ in the flow field can be decomposed into a large-scale parameter $\overline{u}_i(r)$ and a small-scale parameter $u_i'(r)$. The spatial filter averaging is applied to $\overline{u}_i(r)$ as follows

$$\overline{u}(x) = G(|r - r'|)u_i(r)\mathrm{d}r' \tag{2}$$

where $G(|r - r'|)$ is the filter function. The following box filter function is adopted in this paper:

$$G(|r - r'|) = \frac{1}{\sqrt[3]{\Delta_x \Delta_y \Delta_z}},\ |r_j - r_j'| \le \frac{\Delta_j}{2},\ j = x, y, z \tag{3a}$$

$$G(|r - r'|) = 0,\ |r_j - r_j'| > \frac{\Delta_j}{2} \tag{3b}$$

where Δ_j are the spatial filter sizes in x, y, z directions, which are determined by the grid spacings.

When the filter function is applied, the following LES governing equations are obtained:

$$\frac{\partial}{\partial t}\alpha + \nabla \cdot (\alpha \overline{\boldsymbol{v}}) = \frac{m}{\rho_l},\ \nabla \cdot \overline{\boldsymbol{v}} = \left(\frac{1}{\rho_l} - \frac{1}{\rho_v}\right)m,$$

$$\frac{\partial}{\partial t}(\rho \overline{\boldsymbol{v}}) + \nabla \cdot (\rho \overline{\boldsymbol{v}}\,\overline{\boldsymbol{v}}) = -\nabla \overline{p} + \nabla \cdot (\overline{S} - B) \tag{4}$$

where $B = \rho(\overline{\boldsymbol{v}\boldsymbol{v}} - \overline{\boldsymbol{v}}\,\overline{\boldsymbol{v}})$ represents the influence of the small-scale eddies and is the sub-grid stress tensor. The overbar denotes a filtered physical quantity.

A sub-grid viscosity μ_{SGS} can be used to obtain the sub-grid stress tensor according to the Boussinesq hypothesis, so that

$$B = -2\mu_{\mathrm{SGS}}\overline{D} \tag{5}$$

The sub-grid viscosity μ_{sgs} is obtained using the k - μ model:

$$\frac{\partial k_{\mathrm{SGS}}}{\partial t} + \nabla \cdot (k_{\mathrm{SGS}}\overline{\boldsymbol{v}}) = \nabla \cdot \left(\frac{\mu + \mu_{\mathrm{SGS}}}{\rho}\nabla k_{\mathrm{SGS}}\right) + 2\frac{\mu_{\mathrm{SGS}}}{\rho}\overline{D}\overline{D} - C_e\frac{k_{\mathrm{SGS}}^{3/2}}{\overline{\Delta}} \tag{6}$$

$$\mu_{\mathrm{SGS}} = \mathrm{C}_k\overline{\Delta}\sqrt{k_{\mathrm{SGS}}} \tag{7}$$

where k_{SGS} is the SGS turbulent kinetic energy, $\overline{\Delta} = \sqrt[3]{\Delta_x \Delta_y \Delta_z}$ is the size of the average spatial filter, $C_e = 1.048$, $C_k = 0.094$.

1.3 *Structural model*

The RK4, Newmark methods are used to solve the rigid-body motion equation. The structural model adopted in this paper is a rigid circular cylinder mounted on a linear spring in the transverse direction. Thus, the harmonic oscillator equation is used

$$M\ddot{y} + C\dot{y} + Ky = F \tag{8}$$

where M is the structural mass, C is the damping, K is the stiffness, $\ddot{y}$ is the acceleration, $\dot{y}$ is the velocity, y is the displacement of the circular cylinder and F is the external force matrix acted on the circular cylinder.

In the RK4 algorithm, $\ddot{y}$, $\dot{y}$ and y are solved for the next time step as follows:

$$K(\dot{y}, y) = 0,\ T(\dot{y}, y) = \ddot{y} = \frac{F_n - C\dot{y} - Ky}{M},$$

$$K_1 = K(\dot{y}_n, y_n),\ T_1 = T(\dot{y}_n, y_n),$$

$$K_2 = K(\dot{y}_n + 0.5hT_1, y_n + 0.5hK_1),$$

$$T_2 = T(\dot{y}_n + 0.5hT_1, y_n + 0.5hK_1)\cdots,$$

$$y_{n+1} = y_n + \frac{h(K_1 + 2K_2 + 2K_3 + K_4)}{6},$$

$$y_{n+1} = \dot{y}_n + \frac{h(T_1 + 2T_2 + 2T_3 + T_4)}{6} \tag{9}$$

where T_n is the discrete step, h is the time step.

The Newmark method is a numerical method

with a high-order accuracy. However, due to the asynchronous calculation of the rigid-body motion and the flow field, the temporal accuracy of the FSI method used is actually the first-order.

2. Problem definition and verification

2.1 *Problem definition*

A circular cylinder of the mass M and the characteristic diameter $D = 10$ mm is mounted on a linear spring in the transverse direction. Based on the characteristic diameter D and the speed of the free stream U, the Reynolds number Re of the circular cylinder is set as 200. Because the wake flow around a circular cylinder is not strongly three-dimensional when $Re \le 200$, a two-dimensional computational domain is used. To simulate the flow past the freely vibrating circular cylinder, the computational domain is defined as from the inlet at $X = -20D$ to the outlet at $X = 40D$ in the flow direction and from $-20D$ to $20D$ in the transverse direction (Y), as shown in Fig. 2. A velocity inlet condition is applied on the inlet boundary, with the fixed velocity U, and a pressure-outlet condition is applied on the outlet boundary, with the fixed pressure p_∞ determined by the cavitation number $(\sigma = 2(p_\infty - p_v)/(\rho U^2))$. The slip wall conditions are applied on two side boundaries and the circular cylinder is defined as having a no-slip moving wall.

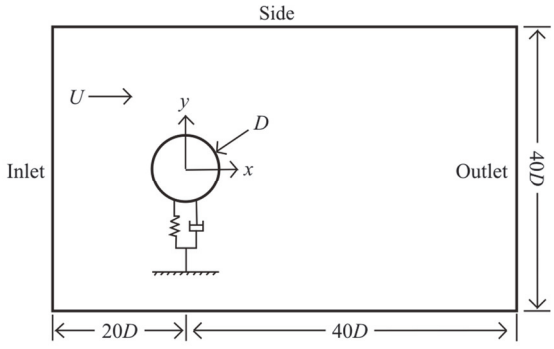

Fig. 2 Computational domain and boundary conditions

A hexahedral-structured grid is employed, while the downstream region of the circular cylinder is refined to simulate the near-wall flow and the vortex evolution accurately. The grid spacing is set as $0.001D \times 0.008D$ in the azimuthal and radial directions near the circular cylinder, stretching to $0.035D \times 0.047D$, $0.06D \times 0.047D$ at distances of $3D$, $7D$ downstream, respectively. The grid number is approximately 6×10^5, and the mesh distributions are shown in Fig. 3. The maximum value of the overall computational domain is less than 1.

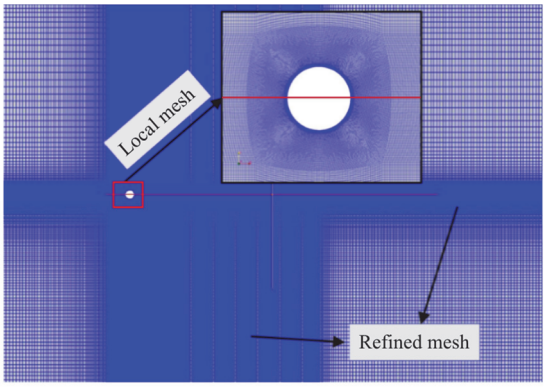

Fig. 3 (Color online) Mesh distributions of the computed domain

2.2 *Verification of FSI method*

A freely vibrating circular cylinder in a free stream with an initial velocity $U = 0$ is simulated to verify the accuracy of the FSI method adopted in this paper. Based on the potential theory, the added mass of the circular cylinder is the mass of the fluid with the same volume in the non-cavitating flow. Using the medium grids and the standard computational domain defined above, and setting the initial state of the circular cylinder as $\ddot{y} = 0$, $\dot{y} = 0$, $y = 0.05D$, The simple harmonic vibration of a circular cylinder in the fully wetted water from a given position is simulated. The fluid force in Eq. (10) can be approximated as an effect of the added mass and the viscous damping.

$$M(1+\rho^*)\ddot{y} + (C + C_f)\dot{y} + Ky = 0 \tag{10}$$

where ρ^* is the density ratio of the solid to the water, C_f is the viscosity coefficient.

In this paper, the effect of the damping of the spring is ignored, so $C = 0$. The dry natural vibrating frequency (F_s) of the circular cylinder in a simple harmonic vibration can then be written as

$$F_s = \frac{1}{2\pi}\sqrt{\frac{K}{M}} \tag{11}$$

where M and K are the structural mass and stiffness.

When the effects of the viscosity are small enough, according to the potential flow theory, the theoretical natural frequency (F_W is the wetted natural vibrating frequency in the non-cavitating flow) of the circular cylinder is

$$F_W = \frac{1}{2\pi}\sqrt{\frac{K}{M(1+1/\rho^*)}} = F_s\sqrt{\frac{1}{1+1/\rho^*}} \tag{12}$$

Three density ratios $\rho^* = 0.5$, 1 and 10 are applied and the resulting values of F_W are shown in Table 1. On the one hand, the computed values of F_W agree well with the theoretical values, which verifies the accuracy of the FSI method adopted in this paper. On the other hand, as the dimensionless density ratio decreases, the deviation between the computed and theoretical results gradually increases, which is related to the viscosity of the water. When the dimensionless density ratio decreases, the kinetic energy of the circular cylinder decreases and the damping effect caused with the viscous force increases.

Table 1 Comparison of natural frequency

No.	ρ^*	Theoretical F_W / F_s	Numerical F_W / F_s	Error
1	10	0.953	0.952	–0.11%
2	1	0.707	0.706	–0.14%
3	0.5	0.577	0.575	–0.34%

The results based on the above numerical method are compared with those in the open literature to further validate the accuracy of the method. Figure 4 shows that the present computed results are in generally good agreement with the results of the experimental measurements conducted by Khalak and Williamson[22] and the simulations accomplished by Guilmineau and Queutey[23]. The results from these three sources have a similar lock-in frequency region corresponding to the range of the reduced speed $(U^* = U^\infty / (F_W \cdot D))$ from about 3 to 12. The considerate difference of the resonance amplitudes may be due to two reasons. On the one hand, the experimental resonance amplitudes exceed the range of the elastic vibration, thus violating the linear elastic vibration assumption in the FSI solver. On the other hand, the initial physical conditions in the experiment and in the simulation are not totally the same. The flow field is uniformly accelerated and then stabilized in the experiment, but the flow field always keeps a constant velocity in the simulation. Some studies[24] have shown that the uniform acceleration movement before the flow field is stable can improve the maximum vibrating amplitude of a circular cylinder in the lock-in frequency region. In a word, we can say that the applied FSI method in the present study is accurate and reliable.

3. Results and discussions

3.1 *Dimensional analysis of control parameters*

The dimensional analysis is conducted for the control parameters of the VIV of a circular cylinder in the cavitating flow. The physical parameters related to the free vibration of a two-dimensional rigid circular cylinder in the cavitating flow can be divided into two parts, those for the fluid system and those for the structural system, as shown in Table 2. In order to analyze the control parameters that affect the vibrating frequency of the circular cylinder, it is necessary to identify those physical parameters that have important influence on the vibration, so to ignore those having less important influence on the vibration.

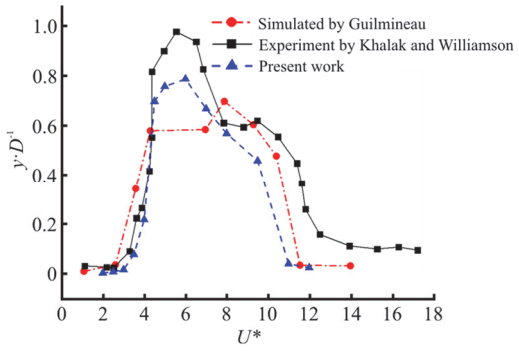

Fig. 4 (Color online) Verification of the FSI methods

Table 2 Main control parameters of the VIV in the cavitating flow

	Parameters
Fluid system	Density of liquid water, vapor ρ_l, ρ_v
	Viscosity coefficient of liquid water, vapor μ_l, μ_v
	Difference between conditional pressure and water saturated vapor pressure $p_\infty - p_v$
	Velocity of flow U_∞
Structural system	Diameter of circular cylinder D
	Density of circular cylinder ρ_s
	Spring stiffness per unit length K

Because the main physical parameter affecting the phase transition in the cavitating flow is the difference between the ambient pressure and the saturated vapor pressure $(p_\infty - p_v)$, which can be combined into one term. In the structural system, the damping has little effect on the vibration frequency. Generally, the density of the vapor is much smaller than that of the liquid, and its dynamic pressure is less important. The viscosity coefficient of the water vapor is much smaller than that of the liquid water, with a very small effect. By combining the arguments above and neglecting the physical parameters with small influence, the relationship between the main control parameters and the vibrating response frequency of a circular cylinder in a two-dimensional cavitating flow can be obtained in a functional form as:

$$f = G(D, U_\infty, \rho_l, \rho_s, K, \mu_l, p_\infty - p_{\text{sat}}) \tag{13}$$

Based on the dimensional analysis, Eq. (13) can be converted to

$$\frac{f}{U_\infty / D} = G\left(\frac{\rho_s}{\rho_l}, \frac{K}{\rho_l U_\infty^2 / 2}, \frac{\mu_l}{\rho_l U_\infty D}, \frac{p_\infty - p_{\text{sat}}}{\rho_l U_\infty^2 / 2}\right) \tag{14}$$

In Eq. (14), U_∞ / D represents the characteristic frequency of the flow. In the flow around the circular cylinder, the vortex shedding frequency F_L of the fixed circular cylinder is the frequency of the fluid force, which can be expressed as $St \cdot U_\infty / D$. In the structural system, the dry natural vibrating frequency F_s of the circular cylinder is $0.5\sqrt{K/M}/\pi$. Through decomposition and combination, the dimensionless parameters are further transformed into more commonly used dimensionless parameters, with clearer physical meaning and more convenient for quantitative analysis. Thus, Eq. (14) can be written as follows:

$$\frac{f}{F_L} = G\left(\frac{\rho_s}{\rho_l}, \frac{F_s}{F_L}, \frac{\mu_l}{\rho_l U_\infty D}, \frac{p_\infty - p_{\text{sat}}}{\rho_l U_\infty^2 / 2}\right) \tag{15}$$

$$f^* = G(\rho^*, F^*, Re, \sigma) \tag{16}$$

where f^* is the dimensionless vibrating frequency, ρ^* is the density ratio, F^* is the frequency ratio, Re is the Reynolds number and σ is the cavitation number. In Eq. (16), the dimensionless vibrating frequency of the circular cylinder is related with four control parameters: ρ^*, F^*, Re and σ. In view of the fact that the resonance effect, the lock-in and other important phenomena in the FSI system are mainly related to the frequency, the present paper mainly studies the influence of the frequency ratio (F^*). The VIV in the cavitating flow is mainly investigated within the range $F^* = 0.5\text{-}3.5$, while the other dimensionless parameters are $\rho^* = 10$, $Re = 200$ and $\sigma = 1$.

3.2 *VIV of a freely vibrating circular cylinder in non-cavitating and cavitating flow*

To investigate the effects of the cavitation on the VIV, the cavitating and non-cavitating flows past a freely vibrating circular cylinder are simulated based on the well-developed flow field described in the above sections. The vortex shedding frequencies of the fixed circular cylinder are $0.2U/D$, $0.18U/D$ in the non-cavitating flow and the cavitating flow, respectively. In this study, the characteristic frequency of the two flows is set as the vortex shedding frequency in the non-cavitating flow, $F_L = 0.2U/D$. The dry natural vibrating frequencies F_s of the circular cylinder are varied in the range from $0.5F_L$ to $3.5F_L$ by changing K.

The variations of the vibrating response frequency and amplitude of the circular cylinder with the increase of F^* in the two flows are shown in Figs. 5, 6, respectively. When F^* is close to 1, the lock-in of the VIV occurs in both flows. In the lock-in frequency range, the vibrating frequencies of the circular cylinder are locked to F_W in the non-cavitating flow, and nearly converge to F_L with the increase of F^*. The dimensionless vibration amplitudes ($A^* = y_{\max} / (0.5\rho U^2 D / K)$) reach the peak values at $F^* = 0.95$, which means the resonances. For frequencies a slightly away from the resonance interval (such as $F^* = 0.7$, 1.2), is affected by the structural vibration and locked to F_s. When $F^* \geq 1.2$, the vortex shedding returns to the original shedding frequency (F_L), and the structural vibration is mainly affected by the vortex shedding frequency. Then, A^* reduces to a value near 1 with the increase of F^*. These conclusions about the simulations of the VIV in the non-cavitating flow are in good agreement with the previous research[25].

The difference of the vibration in the cavitating and non-cavitating flows is now the focus point. As shown in Fig. 5, the lock-in frequency range in the cavitating flow ($1.5 \geq F^* \geq 0.5$) is larger than that in the non-cavitating flow ($1.2 \geq F^* \geq 0.5$). When F^* is beyond the lock-in frequency range, the vibrating frequency of the circular cylinder in the cavitating flow (approximately $0.9F_L$) is smaller than that in the non-cavitating flow (F_L). As it is seen from Fig. 6, that in the lock-in frequency range, the vibrating amplitude of the circular cylinder in the non-cavitating flow is significantly larger than that in the cavitating flow, in the range ($1.2 \geq F^* \geq 0.5$), then it becomes smaller in the range ($2.0 \geq F^* \geq 1.25$). In summary, the cavitation increases the range of the VIV lock-in frequencies and reduces the vibrating amplitude in the lock-in frequency range. The mechanisms of these phenomena can be revealed from the frequencies and the displacements of the vibration in the lock-in frequency range.

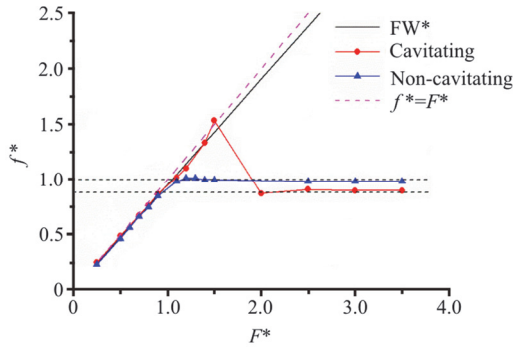

Fig. 5 (Color online) Vibrating frequencies of a circular cylinder with different F^* in cavitating and non-cavitating flows

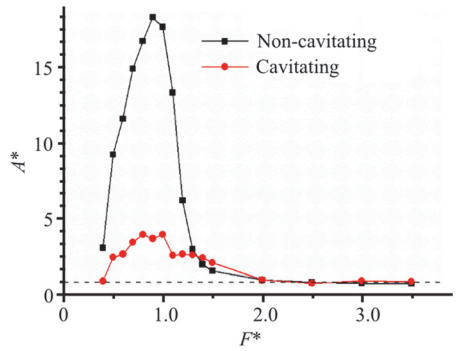

Fig. 6 (Color online) Vibration amplitudes of a circular cylinder with different F^* in cavitating and non-cavitating flows

3.3 *Analysis of the effects of cavitation on VIV*

To investigate the mechanisms of the cavitation effects conveniently and directly, the flow structures and the vibrating displacements of the circular cylinder are compared and analyzed at $F^*=0.9$, 1.2 ($F^*=1.0$ means that F_s is equal to F_L). From Eq. (14), $F_W=0.95F_s$. The resonance is clearly observed around $F^*=0.9$: The vibration amplitudes of the circular cylinder in both flows almost reach their peak values, so this scenario is convenient for comparing and analyzing the effects of cavitation on the vibrating amplitude of the circular cylinder in the lock-in frequency range. On the other hand, as shown in Fig. 6, F^* in the lock-in frequency range ranges from 0.5 to 1.2 in the non-cavitating flow, which is a smaller range than that in the cavitating flow (from 0.5 to 1.5). Therefore, the flow structures and the vibrating displacements at $F^*=1.2$ are selected to analyze the effects of cavitation on the vibrating frequency of the circular cylinder in the lock-in frequency region.

3.3.1 Decrease of vibrating amplitude in the lock-in frequency range induced by cavitation

In the lock-in frequency range, the vortex structures in the wake of the circular cylinder at $F^*=0.9$ see differences between the non-cavitating and cavitating flows. The vortex is represented by using the Q-criterion[26], defined as Eq. (17), in Fig. 7. The solid black line in Fig. 7(a) is a streamline showing the flow direction and the solid black line in Fig. 7(b) is the iso-surface of $\alpha=0.9$, representing the vapor in a cavitation. The $2S$ model[27] vortex shedding can be found in both the non-cavitating and cavitating flows. Meanwhile, the distances between the vortices in the cavitating flow in both the transverse and flow directions are smaller, and the vortices are stronger.

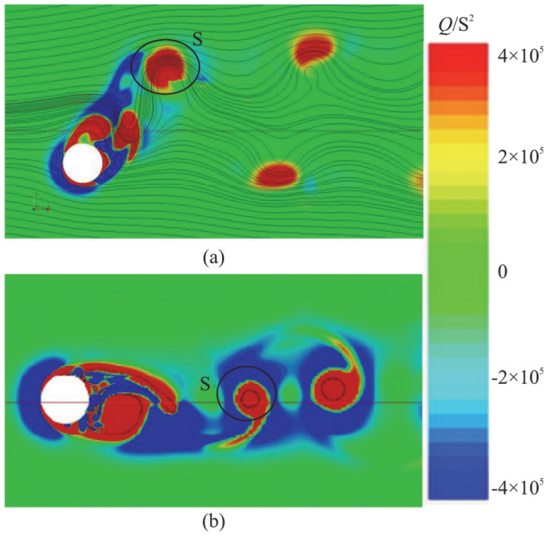

Fig. 7 (Color online) Vortex structures in the non-cavitating (a) and cavitating (b) flows at $F^*=0.9$

In the incompressible flow, Q is defined as

$$Q=0.5\times(\|\boldsymbol{\Omega}\|^2-\|D\|^2) \tag{17}$$

where $\boldsymbol{\Omega}$ represents the vorticity tensor, D represents the strain rate tensor and Q has a direct physical meaning, when $Q\geq 0$, the vector field is dominated by the vorticity, and the region can be described as a vortex tube, whereas, when $Q<0$, the vector field is dominated by the strain.

The circular cylinder vibrates with a single frequency F_W and a steady amplitude in the non-cavitating flow, as shown in Fig. 8. The maximum value of the vibration displacement is about $0.8D$, and the frequency is $0.94F_s$, which is close to F_W. The vortex shedding frequency in the wake is no longer F_L but becomes the same as F_W of the

circular cylinder, which is defined as the lock-in frequency. The vortex shedding frequency is synchronized with the vibrating frequency of the circular cylinder, and the $2S$ model shedding vortices can be seen in Fig. 7(a). In the cavitating flow, with unstable vibration amplitudes and the maximum value less than $0.2D$, and with a broader frequency spectrum, as shown in Fig. 9. The lock-in phenomenon also occurs, and the $2S$ model shedding vortices can be seen in Fig. 7(b). From the differences of the vibrating displacements of the circular cylinder in the non-cavitating and cavitating flows, we can deduce that it is the unsteady and high-frequency characteristics of the cavitation that causes the unsteady vibration, with a broader frequency spectrum. The constraints of the cavitating flow on the circular cylinder are weaker, and the cavitation evolution, especially, the collapse, brings about a high-frequency pressure fluctuation, to increase the instability of the systems, which makes a strong resonance less likely to occur, i.e., the cavitation reduces the VIV resonance effect. In addition, the transverse fluid force on the circular cylinder at the dominant frequency in the cavitating flow is significantly smaller[25], so the vibration amplitudes of the circular cylinder in the cavitating flow are significantly smaller in the lock-in frequency range.

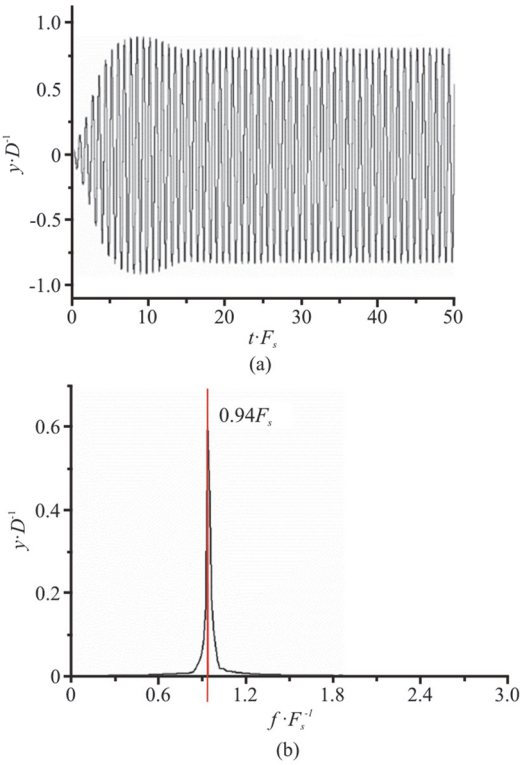

Fig. 8 (Color online) Computed results (a) and FFT results (b) of vibration amplitudes in the non-cavitating flow at $F^* = 0.9$

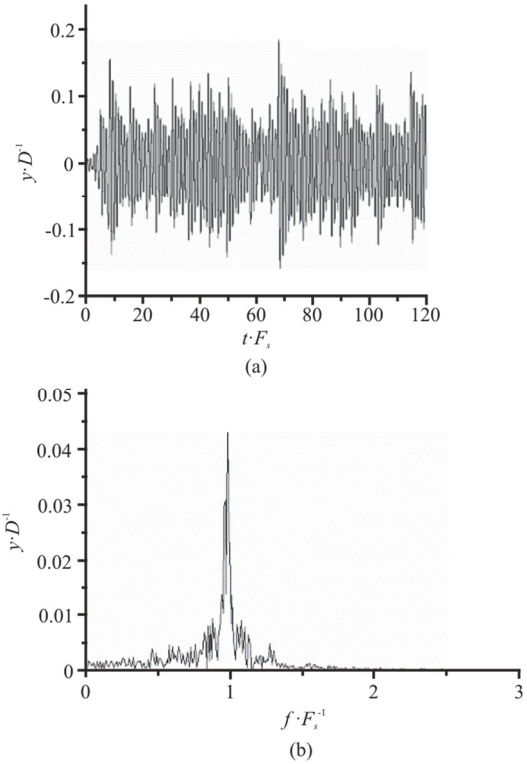

Fig. 9 Computed results (a) and FFT results (b) of vibration amplitudes in the cavitating flow at $F^* = 0.9$

3.3.2 Increase of the lock-in frequency range induced by cavitation

At $F^* = 1.2$, the dry natural vibrating frequency of the circular cylinder in the non-cavitating flow is larger than the vortex shedding frequency. As shown in Fig. 10, the $2S$ model vortex shedding can again be observed in both the non-cavitating and cavitating flows. However, the shedding vortices in the cavitating flow are not as coherent as those in the non-cavitating flow. Some small vortices are shed according to the $2S$ model, as shown in Fig. 10(b), induced by the vibration and the cavitation.

From Fig. 11, the vibrating amplitude of the circular cylinder approaches a stable value of $0.18D$. Unlike the case at $F^* = 0.9$, a clear "beat" phenomenon is observed in the first 50 cycles, when the circular cylinder begins to vibrate and two components corresponding to F_L, F_W can be identified in the FFT results. The "beat" phenomenon is the superposition of the two components in the spectrum, as responsible for the "beat" phenomenon in the initial stage. Therefore, the FFT is performed separately for the first 50 cycles and the subsequent stable stage.

As shown in Fig. 12, the circular cylinder in the non-cavitating flow vibrates in two phases: the initial phase $t \cdot F_s = (0,50)$ and the stable phase $t \cdot F_s = (60,$

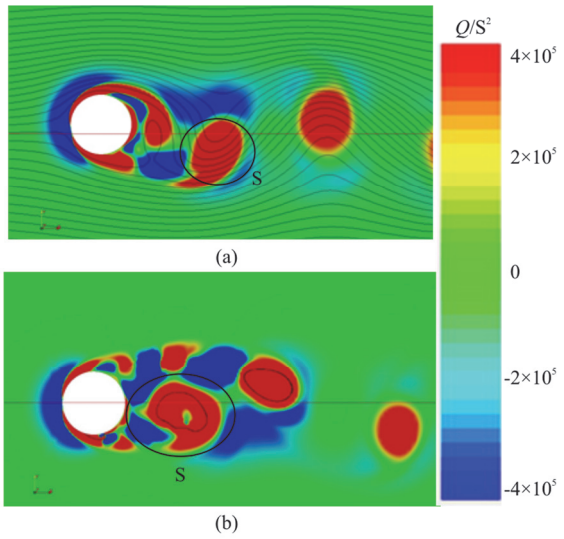

Fig. 10 (Color online) Vortex structure in the non-cavitating flow (a) and the cavitating flow (b) at $F^* = 1.2$

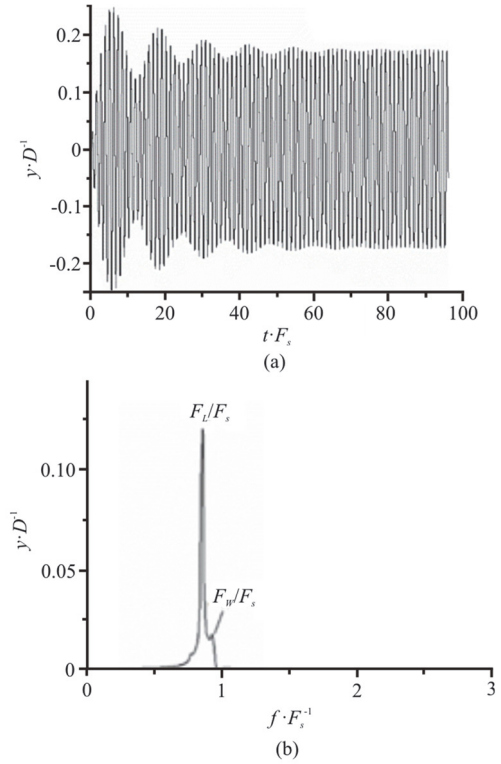

Fig. 11 Computed results (a) and FFT results (b) of vibrating displacements in the non-cavitating flow at $F^* = 1.2$

100). During the initial phase, one sees clearly two components (F_L, F_W), because the vibration is not synchronized with the wake over the circular cylinder. During the stable stage, the circular cylinder vibrates with a single frequency (F_L) and a steady amplitude indicating that the vibrating frequency of the circular cylinder is locked to the vortex shedding frequency and the circular cylinder vibrates under the fluid force, with a natural flow frequency F_L, as a forced vibration. With a combined consideration of the vortex structures in the flow field, it is found that the vibration of the circular cylinder is synchronized with the vortex shedding in a later fluttering stage, to form the $2S$ vortex structure, as shown in Fig. 10(a). From the above analysis, it is seen that when F^* is sufficiently large ($F^* \geq 1.2$), at the upper end of the lock-in frequency range, the circular cylinder will be in a forced vibration under the fluid force with the frequency F_L in the non-cavitating flow. The component of the wetted natural vibrating frequency of the circular cylinder disappears under the restraint of the flow.

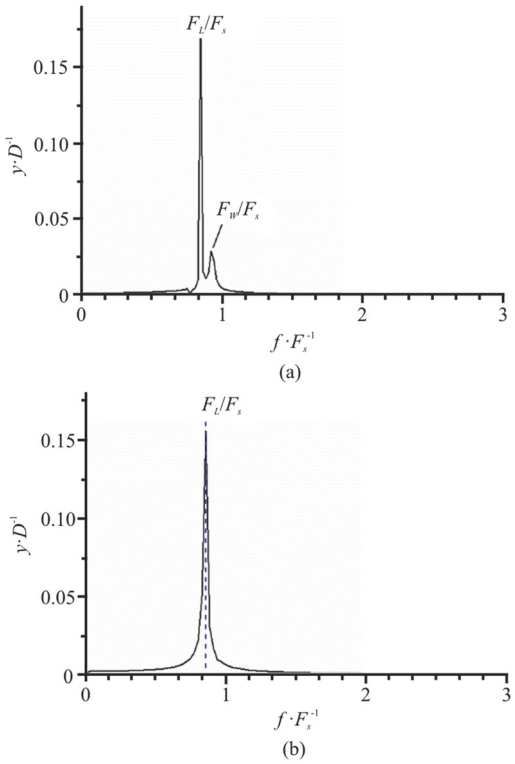

Fig. 12 (Color online) FFT results of vibrating displacements in the initial a and stable b phases in the non-cavitating flow at $F^* = 1.2$

At $F^* = 1.2$, the circular cylinder will not be in the forced vibration in the cavitating flow, and will vibrate with a unstable amplitude and with more frequency components, as shown in Fig. 13. The observed two most representative frequency components are F_W, $1.1F_L$. Compared with the cavitation shedding frequency ($0.9F_L$) of a fixed circular cylinder, the characteristic frequency ($1.1F_L$) of the

fluid force of a freely vibrating circular cylinder is significantly greater, showing that the vibrating amplitude of the circular cylinder is small but it still has a clear influence on the flow. As shown in Fig. 10(b), under the influence of vibration of the circular cylinder and the oscillation of the collapsed bubble, the shedding vortex in the cavitating flow is unstable, and is more vulnerable to the structural vibration. In the lock-in frequency range, although the cavity shedding frequency, affected by the structural vibration, is close to the vibrating frequency, the lock-in occurs with a weak constraint because the unstable and pressure-sensitive cavity shedding frequency does not easily synchronize fully with the vibrating frequency of the circular cylinder. In contrast, the low-density vapor around the circular cylinder weakens constraints of the flow, and the natural vibrating frequency of the circular cylinder in the cavitating flow decreases more slowly with the increasing frequency ratio. Therefore, the forced vibration is delayed by the cavitation, and the lock-in frequency range expands in the cavitating flow.

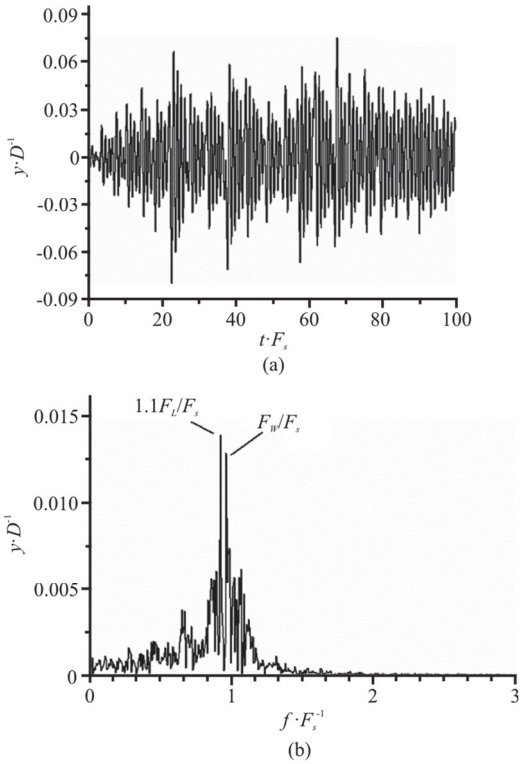

Fig. 13 Computed results (a) and FFT results (b) of vibrating displacements in the cavitating flow at $F^* = 1.2$

4. Conclusions

In the present paper, the effects of the cavitation on the vortex-induced vibration of a circular cylinder are investigated by an in-house FSI solver in the OpenFOAM framework. The conclusions are as follows:

(1) For a freely vibrating circular cylinder, the VIV lock-in is observed both in the non-cavitating flow and the cavitating flow. The lock-in frequency range $(1.5 \geq F^* \geq 0.5)$ in the cavitating flow is larger than that $(1.2 \geq F^* \geq 0.5)$ in the non-cavitating flow, and the vibration amplitude of the circular cylinder in the lock-in frequency range is clearly smaller in the cavitating flow.

(2) The vibration amplitude of the structure is far smaller in the lock-in frequency range in the cavitating flow. The fluid force at the dominant frequency (the vortex shedding frequency) is smaller. The low-density cavitation area around the circular cylinder weakens the effect of the flow on the structure, and the cavitation collapse makes it difficult for the vibrations of the flow and the structure to be completely synchronized, so that the resonance effect is weakened. Therefore, the vibrating amplitude of the circular cylinder in the cavitating flow is significantly smaller in the lock-in frequency range. On the other hand, the natural vibrating frequency decreases more slowly with the increase of the frequency ratio, because the effect of the flow on the circular cylinder is smaller in the cavitating flow. Furthermore, the collapse of the cavitation weakens the stability of the shedding vortices and therefore the flow around the circular cylinder is more sensitive to the structural vibration. Consequently, the lock-in frequency range is larger in the cavitating flow.

Acknowledgment

This work was supported by theYouth Innovation Promotion Association, Chinese Academy Sciences (Grant No. Y201906).

References

[1] Shi Y., Pan G., Yan G. X. et al. Numerical study on the cavity characteristics and impact loads of AUV water entry [J]. *Applied Ocean Research*, 2019, 89: 44-58.

[2] Liu G., Li H., Xie Y. et al. Investigating cross-flow vortex-induced vibration of top tension risers with different aspect ratios [J]. *Ocean Engineering*, 2021, 221: 108497.

[3] Kan K., Zheng Y., Chen H. et al. Study into the improvement of dynamic stress characteristics and prototype test of an impeller blade of an axial-flow pump based on bidirectional fluid–structure interaction [J]. *Applied Sciences*, 2019, 9(17): 3601.

[4] Cheng Y., Oertel H., Schenkel T. Fluid-structure coupled CFD simulation of the left ventricular flow during filling phase [J]. *Annals of Biomedical Engineering*, 2005, 33(5): 567-576.

[5] Wang T., Zhou W., Chen J. et al. Simulation of hydraulic

fracturing using particle flow method and application in a coal mine [J]. *International Journal of Coal Geology*, 2014, 121: 1-13.

[6] Liu Z. G., Liu Y., Lu J. Fluid–structure interaction of single flexible cylinder in axial flow [J]. *Computers and Fluids*, 2011, 56: 143-151.

[7] Bai X. R., Cheng H. Y., Ji B. et al. Spatial and spectral investigation of turbulent kinetic energy in cavitating flow generated by Clark-Y hydrofoil [J]. *Journal of Hydrodynamics*, 2020, 32(1): 175-178.

[8] Gabbai R. D., Benaroya H. An overview of modeling and experiments of vortex-induced vibration of circular cylinders [J]. *Journal of Sound and Vibration*, 2004, 282(3-5): 575-616.

[9] Kang Z., Zhang C., Chang R. A higher-order nonlinear oscillator model for coupled cross-flow and in-line VIV of a circular cylinder [J]. *Ships and Offshore Structures*, 2018, 13(5): 1-16.

[10] Khan N. B., Ibrahim Z. VIV study of an elastically mounted circular cylinder having low mass-damping ratio using RANS model [J]. *International Journal of Heat and Mass Transfer*, 2018, 121: 309-314.

[11] Shi H., Zhou D., Wen J. Fluid-solid interaction simulation of elastic cylindrical shell penetrating water based on the ALE method [J]. *Journal of Ballistics*, 2020, 32(1): 9-14.

[12] Sun T., Li Z., Yin Z. et al. Cavitation bubble dynamics and structural loads of high-speed water entry of a cylinder using fluid-structure interaction method [J]. *Applied Ocean Research*, 2020, 64: 101-137.

[13] Gao Y., Sun T., Zhang G. et al. Flow characteristics and structure response of high-speed oblique water-entry for a revolution body [J]. *Explosion and Shock Waves*, 2020, 40(12): 177-203.

[14] Kaolan P., Lehman A. F. Experimental studies of hydroelastic instabilities of cavitation hydrofoils [J]. *Journal of Aircraft*, 2015, 3(3): 262-269.

[15] Akcabay D. T., Chae E. J., Yin L. Y. Cavity induced vibration of flexible hydrofoils [J]. *Journal of Fluids and Structures*, 2014, 49(8): 463-484.

[16] Akcabay D. T., Young Y. L. Influence of cavitation on the hydroelastic stability of hydrofoils [J]. *Journal of Fluids and Structures*, 2014, 49: 170-185.

[17] Sareen A., Zhao J., Jacono D. L. Vortex-induced vibration of a rotating sphere [J]. *Journal of Fluid Mechanics*, 2018, 837: 258-292.

[18] Torre O., Escaler X., Egusquiza E. Experimental investigation of added mass effects on a hydrofoil under cavitation conditions [J]. *Journal of Fluids and Structures*, 2013, 39: 173-187.

[19] Ducion A., Astolfi J. A., Sigrist J. F. et al. An experimental analysis of fluid structure interaction on a flexible hydrofoil in various flow regimes including cavitating flow [J]. *European Journal of Mechanics*, 2012, 36: 63-74.

[20] Kunz R. F., Boger D. A., Stinebring D. R. A preconditioned Navier–Stokes method for two-phase flows with application to cavitation prediction [J]. *Computers and Fluids*, 2000, 29(8): 849-875.

[21] Wang Y., Liao L., Du T. et al. A study on the collapse of cavitation bubbles surrounding the underwater-launched projectile and its fluid–structure coupling effects [J]. *Ocean Engineering*, 2014, 84: 228-236.

[22] Khalak A., Williamson C. Motions, forces and mode transitions in vortex-induced vibrations at low mass-damping [J]. *Journal of Fluids and Structures*, 1999, 13(7-8): 813-851.

[23] Guilmineau E., Queutey P. Numerical simulation of vortex-induced vibration of a circular cylinder with low mass-damping in a turbulent flow [J]. *Journal of Fluids and Structures*, 2004, 19(4): 449-466.

[24] Yao W., Jaiman R. K. Model reduction and mechanism for the vortex-induced vibrations of bluff bodies [J]. *Journal of Fluid Mechanics*, 2017, 827: 357-393.

[25] Wen C. Y., Lin C. Y. Two-dimensional vortex shedding of a circular cylinder [J]. *Physics of Fluids*, 2001, 13(3): 557-560.

[26] Huang R., Luo X., Ji B. Numerical simulation of the transient cavitating turbulent flows around the Clark-Y hydrofoil using modified partially averaged Navier-Stokes method [J]. *Journal of Mechanical Science and Technology*, 2017, 31(6): 2849-2859.

[27] Langre E. D. Frequency lock-in is caused by coupled-mode flutter [J]. *Journal of Fluids and Structures*, 2006, 22(6-7): 783-791.